

Reduced order modeling with Barlow Twins self-supervised learning: Navigating the space between linear and nonlinear solution manifolds

Teeratorn Kadeethum^{1,2}, Francesco Ballarin³, Daniel O'Malley⁴, Youngsoo Choi⁵, Nikolaos Bouklas^{2,*}, and Hongkyu Yoon^{1,*}

¹Sandia National Laboratories, New Mexico, USA

²Cornell University, New York, USA

³Catholic University of the Sacred Heart, Brescia, Italy

⁴Los Alamos National Laboratory, New Mexico, USA

⁵Lawrence Livermore National Laboratory, California, USA

*nbouklas@cornell.edu, hyoon@sandia.gov

ABSTRACT

We propose a unified data-driven reduced order model (ROM) that bridges the performance gap between linear and nonlinear manifold approaches. Deep learning ROM (DL-ROM) using deep-convolutional autoencoders (DC-AE) has been shown to capture nonlinear solution manifolds but fails to perform adequately when linear subspace approaches such as proper orthogonal decomposition (POD) would be optimal. Besides, most DL-ROM models rely on convolutional layers, which might limit its application to only a structured mesh. The proposed framework in this study relies on the combination of an autoencoder (AE) and Barlow Twins (BT) self-supervised learning, where BT maximizes the information content of the embedding with the latent space through a joint embedding architecture. Through a series of benchmark problems of natural convection in porous media, BT-AE performs better than the previous DL-ROM framework by providing comparable results to POD-based approaches for problems where the solution lies within a linear subspace as well as DL-ROM autoencoder-based techniques where the solution lies on a nonlinear manifold; consequently, bridges the gap between linear and nonlinear reduced manifolds. We illustrate that a proficient construction of the latent space is key to achieving these results, enabling us to map these latent spaces using regression models. The proposed framework achieves a relative error of 2% on average and 12% in the worst-case scenario (i.e., the training data is small, but the parameter space is large.). We also show that our framework provides a speed-up of 7×10^6 times, in the best case, and 7×10^3 times on average compared to a finite element solver. Furthermore, this BT-AE framework can operate on unstructured meshes, which provides flexibility in its application to standard numerical solvers, on-site measurements, experimental data, or a combination of these sources.

Introduction

A reduced order model (ROM) is devised to provide an acceptable accuracy while utilizing a much lower computational cost compared to the full order model (FOM)¹. In recent years, a non-intrusive or data-driven ROM approach has grasped attention because (1) it has a straightforward implementation (i.e., does not require any modifications of FOM), (2) it easily lends itself to different kinds of physical problems, and (3) it allows for more stable and much faster prediction than intrusive ROM for nonlinear problems²⁻⁵. Traditionally, proper orthogonal decomposition (POD) is used as a data compression tool (i.e., linear subspace approach), which is the optimal way to construct the linear reduced manifolds. However, POD-based solutions on a linear subspace are often restrictive for highly nonlinear problems where reduced spaces lie in nonlinear manifolds. More recently, nonlinear compression using autoencoder-based deep learning (DL) architectures or nonlinear manifold approach^{3,4,6-8} has been suggested to reconstruct these nonlinear manifolds, resulting in generic and more refined predictive capabilities than linear subspace approaches for nonlinear problems. Recent extensive comparisons, however, show a performance deficit for DL-ROM approaches in some cases⁴.

Kadeethum et al.⁴ illustrate that there are two essential issues for DL-ROM. First, the nonlinear approach outperforms its linear counterpart in specific settings (e.g., boundary conditions and domain geometry), but the opposite can occur in other settings. This is because POD provides the optimal data compression in a linear subspace for the problems with fast-decaying Kolmogorov's n -width that measures the degree of accuracy by n -dimensional linear subspaces⁹⁻¹². Therefore, the DL-ROM approach could not exceed the level of POD accuracy for problems that naturally lie within linear manifolds. However, for

problems with slowly decaying Kolmogorov's width, the nonlinear manifold approach outperforms the linear subspace one. Even though the authors hypothesize that a visual comparison between principal component analysis (PCA) and t-Distributed Stochastic Neighbor Embedding (t-SNE) could indicate which method will perform better before employing any specific compression strategy, there is no unified model that could be used across problem settings without an extensive case-based hyperparameter search. Second, although the nonlinear approach excels in very complex settings, it relies on convolutional operators, hindering its application for unstructured meshes and limiting DL-ROM approaches to less practical problems. Hence, these limitations in DL-ROM methods need to be resolved and tested with varying degrees of complex problems.

The problem of natural convection in porous media is important in various engineering applications ranging from geothermal energy, seawater intrusion, contaminant transport to the storage of nuclear and radioactive waste^{13–16}. Changes in the porous media temperature or fluid concentration result in variations in fluid density and viscosity that could, in turn, regulate the fluid flow field through flow instabilities or, in severe case fingering^{17–19}. Typically, the problem behavior is characterized by the dimensionless Rayleigh number (Ra), indicating laminar or turbulent flow regimes. The higher Ra, the higher chances that flow instability occurs. One of many practical examples of interest is the process of carbon dioxide (CO₂) sequestration in aquifers. Depending on system Ra and the formation of heterogeneity, convective mixing can greatly accelerate CO₂ dissolution during geologic carbon storage^{20–22}.

To mimic the problem of natural convection in porous media, we utilize the mixed finite element method and interior penalty enriched Galerkin approximation for the spatial discretization and the 4th-order backward differentiation formula for time-stepping as our full order model (FOM), as previously implemented by the authors^{23,24}. This FOM guarantees the local mass conservation and accurately captures the gravity-driven flow in the advection-dominated regime^{24–26}. This FOM, however, is computationally expensive since the problem is highly nonlinear. Furthermore, to investigate the system dynamics for a longer time, the FOM needs to go through very small intermediate time-steps to satisfy the Courant–Friedrichs–Lewy (CFL) condition^{27–29}. Hence, the FOM is not practical in engineering applications such as parameter estimation, real-time system monitoring and control, or energy production optimization because an extensive set of parameter space must be explored^{1,30–34}.

Kadeethum et al.⁴ propose a data-driven reduced order model (ROM) that can reduce computation cost while maintaining an acceptable accuracy for natural convection in porous media problems. The model is applicable to parameterized problems^{1,12,34–39}, depending on a set of parameters (μ) which could correspond to physical properties, geometric characteristics, or boundary conditions. This model sequentially follows (1) the offline and (2) online stages^{1,40}. The offline stage begins with initializing a set of input parameters, which we call a training set. Then the FOM is solved corresponding to each member in the training set (in the following, we will refer to the corresponding solutions as snapshots). Either linear, relying on POD,^{2,41} or nonlinear compression, depending on deep convolutional autoencoder (DL-AE or DL-ROM)^{3,4,7}, is then used to compress FOM snapshots to produce basis functions that span reduced spaces of very low dimensionality, but still guarantee accurate reproduction of the snapshots^{42,43}. The ROM can then be solved during the online stage for any new value of μ by seeking an approximated solution in the reduced space.

In this work, we propose a unified data-driven ROM using a combination of Barlow Twins (BT) self-supervised learning and an autoencoder (BT-AE) that bridges the performance gap between linear and nonlinear manifold approaches. In particular, we use BT self-supervised learning to maximize the information content of the embedding with the latent space through a joint embedding architecture⁴⁴. With four different example cases that span the degree of complexity to cover both linear and nonlinear problems, a comparison of the proposed BT-AE framework with both linear (POD) and nonlinear (DL-AE) ROM approaches is conducted to demonstrate the performance of the unified data-driven ROM framework that (1) excels in all test cases (whether the solution can be captured in a linear or nonlinear manifold) and (2) operates on either structured or unstructured meshes. Importantly, this model is fully data-driven; it could be trained by data produced by FOM, on-site measurement, experimental data, or a combination of them. This characteristic can provide flexibility across the spectrum in more complex problems. Since it is not limited by the Courant–Friedrichs–Lewy condition for conventional FOMs, it could deliver quantities of interest at any given time contrary to the FOM⁴.

Results

Data generation

We present a summary of all geometries and boundary conditions we use in Figure 1. In short, Examples 1, 2, and 3 represent cases where μ is a scalar quantity, namely Ra, while Example 4 illustrates a case where μ is a four-dimensional vector, composed of Ra₁, Ra₂, Ra₃, and Ra₄. The details of each example and their physical interpretations and relevance will be discussed in the following subsections. The information of each example is presented in Table 1. For compactness, throughout this section, we will focus on the results of the temperature field. This is also an advantage of non-intrusive ROMs for coupled multiphysical processes because it can selectively focus only on the quantities of interest. For instance, if we are interested in the temperature field of the gravity-driven flow in porous media problems, we can build our non-intrusive ROM for the temperature field without necessarily carrying on the construction of the ROM for pressure and velocity fields. We note that

$M_{\text{validation}}$ and M_{test} represent the number of the validation and testing sets with varying Rayleigh number (Ra), respectively (Table 1). Due to time dependence, the total number of training, validation, and test samples is the product of M and N^t with varying N^t ranges. Specifically the validation samples, $M_{\text{validation}}N^t$, is determined by $M_{\text{validation}}N^t = 0.1MN^t$ by randomly sampling 10% of the sum of training/validation sets (MN^t).

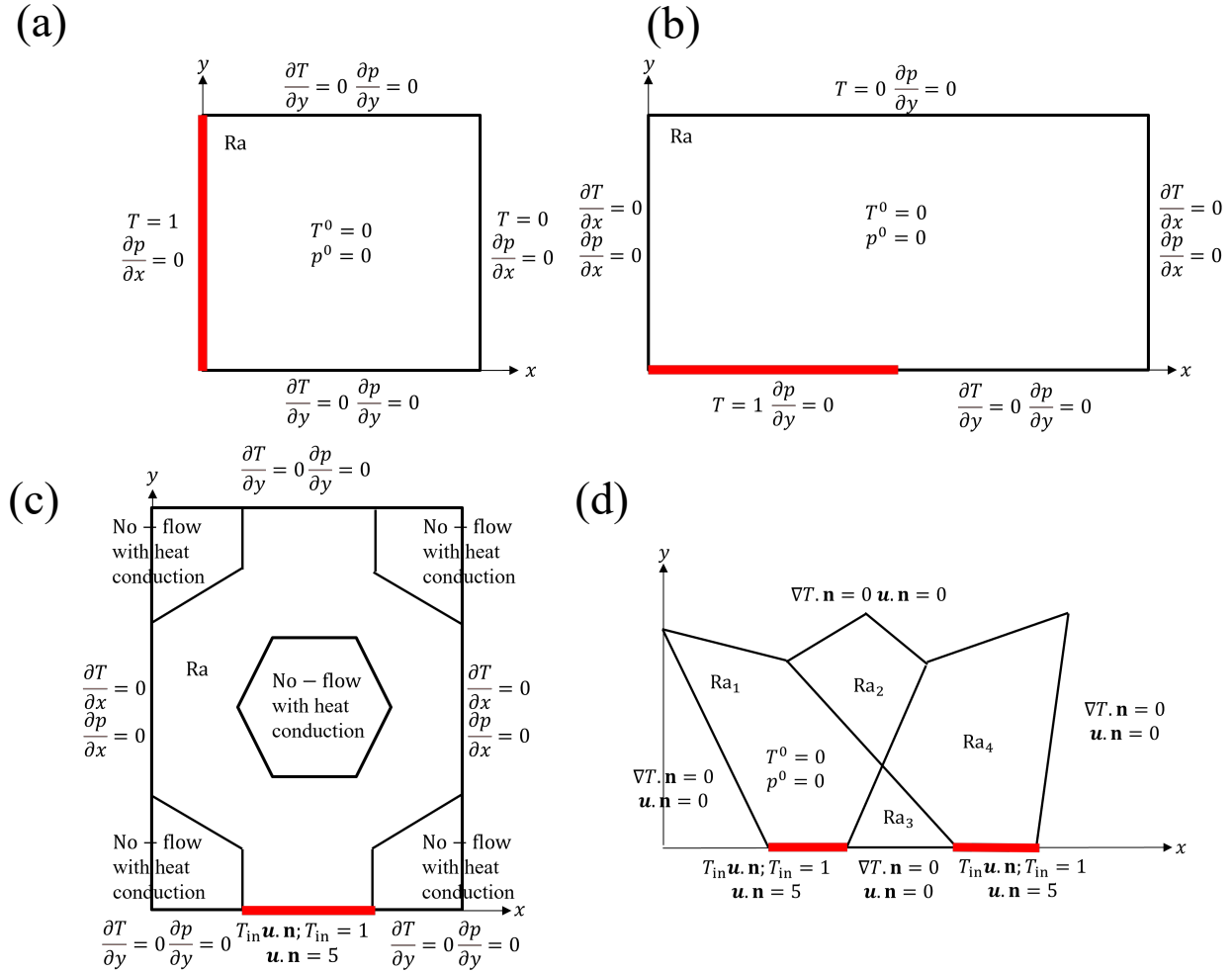


Figure 1. Domain and boundary conditions for (a) Example 1 (heating from the left boundary), (b) Example 2 (Elder problem), (c) Example 3 (unit cell of micromodel), and (d) Example 4 (modified Hydrocoin with four subdomains). The red line indicates the region of the boundary where the temperature is elevated.

The summary of each model, including the subspace dimension and compression method, is presented in Table 2. The detailed description of POD, AE, and DC-AE models is provided in Kadeethum et al.⁴, and our newly developed BT-AE models are described in the **Methodology** section. In short, for POD models, we use proper orthogonal decomposition as a compression tool. The AE models use an autoencoder as a compression method. We employ a deep convolutional autoencoder to compress our training snapshots (MN^t) for DC-AE models. The BT-AE models utilize a combination of an autoencoder and Barlow Twins self-supervised learning in their compression procedure. For the POD models, linear compression, subspace dimension refers to the number of reduced basis or N as well as the number of intermediate reduced basis or N_{int} . We assume $N = N_{\text{int}}$ for all models for simplicity. The subspace dimension is the number of latent space (Q) for the nonlinear compression, AE, DC-AE, and BT-AE models.

Comparisons of BT-AE with POD, AE, and DC-AE models in simple domains

We first compare the BT-AE model accuracy (for different numbers of Q) with the models developed by Kadeethum et al.^{4,41} (i.e., POD, AE, and DC-AE models) in relatively simple model domains. Example 1 illustrates a case where a linear manifold is optimal, while Example 2 presents a case where a nonlinear manifold is optimal. The results of POD, AE, and DC-AE models

Table 1. Summary of main information for each example.

	Example 1	Example 2	Example 3	Example 4	remark
M	40	40	40	81	training set for the parameter space $\boldsymbol{\mu}$
$M_{\text{validation}}N^t$	10% of MN^t	10% of MN^t	10% of MN^t	10% of MN^t	validation set - randomly select from MN^t
M_{test}	10	10	10	10	test set for the parameter space $\boldsymbol{\mu}_{\text{test}}$
MN^t	16802	36110	44354	90175	total training/validation data
$M_{\text{test}}N^t$	3260	8951	11238	11432	total testing data
N^t range	[226, 477]	[790, 1010]	[951, 1265]	[907, 1280]	for training, validation, and test sets
N_h^t	7110	9600	17064	11382	degree of freedom (DOF): T_h
t range	[0.0, 0.1]	[0.0, 0.1]	[0.0, 0.1]	[0.0, 0.1]	$[t^0, t^N]$
$\boldsymbol{\mu}$	$Ra \in [40, 80]$	$Ra \in [350, 450]$	$Ra \in [350, 450]$	$Ra_1 \in [350, 450]$ $Ra_2 \in [350, 450]$ $Ra_3 \in [350, 450]$ $Ra_4 \in [350, 450]$	only Example 4 has four parameters

It is noted that the final total training samples are $0.9MN^t$ because we allocate 10% of the training samples for the validation set. The total of testing data is $M_{\text{test}}N^t$. We want to emphasize that our N^t is not constant, but it is a function of $\boldsymbol{\mu}$. To elaborate, the higher Ra value will result in the higher N^t to satisfy CFL condition.

Table 2. Summary of naming for each model.

model name	compression	subspace dimension	compression techniques
POD 16 RB	linear	16	proper orthogonal decomposition
POD 50 RB	linear	50	proper orthogonal decomposition
POD 100 RB	linear	100	proper orthogonal decomposition
POD 500 RB	linear	500	proper orthogonal decomposition
AE 4 Q	nonlinear	4	autoencoder
DC-AE 4 Q	nonlinear	4	deep convolutional autoencoder
BT-AE 4 Q	nonlinear	4	Barlow twins + autoencoder
AE 16 Q	nonlinear	16	autoencoder
DC-AE 16 Q	nonlinear	16	deep convolutional autoencoder
BT-AE 16 Q	nonlinear	16	Barlow twins + autoencoder
AE 256 Q	nonlinear	256	autoencoder
DC-AE 256 Q	nonlinear	256	deep convolutional autoencoder
BT-AE 256 Q	nonlinear	256	Barlow twins + autoencoder

Details of POD, AE, DC-AE models are provided in Kadeethum et al.⁴.

presented in Kadeethum et al.⁴ demonstrated that the POD-based and DL-ROM approaches are more suitable for the linear and nonlinear manifold problems, respectively, and they are used in this manuscript to evaluate the performance of BT-AE models.

Example 1: Heating from the left boundary

The geometry and boundary conditions are shown in Figure 1a, and we adopt this example from Zhang et al. and Kadeethum et al.^{4,25}. This example represents a case where its fluid flow is driven by buoyancy as the fluid is heated on the left side of the domain. The fluid then flows upwards and rotates to the right side of the domain. We set $\boldsymbol{\mu} = (Ra)$, and its admissible range of variation is [40.0, 80.0], see Table 1. For the training set, we use $M = 40$, which lead to, in total, $MN^t = 16802$ training data points.

We present the test case results of the BT-AE model (BT-AE 16 Q) as supplemental information (SI-Animation-Example 1). The difference between solutions produced by the FOM and ROM (DIFF) is calculated by

$$\text{DIFF}_{\varphi}(t^k, \boldsymbol{\mu}_{\text{test}}^{(i)}) = \left| \varphi_h(\cdot; t^k, \boldsymbol{\mu}_{\text{test}}^{(i)}) - \widehat{\varphi}_h(\cdot; t^k, \boldsymbol{\mu}_{\text{test}}^{(i)}) \right| \quad (1)$$

where φ_h is a finite-dimensional approximation of the set of primary variables corresponding to velocity, pressure, and temperature fields. $\widehat{\varphi}_h$ is an approximation of φ_h produced by the ROM. Thus, $\varphi_h(\cdot; t^k, \boldsymbol{\mu}_{\text{test}}^{(i)})$ and $\widehat{\varphi}_h(\cdot; t^k, \boldsymbol{\mu}_{\text{test}}^{(i)})$ represent φ_h and

$\widehat{\varphi}_h$ at all space coordinates (i.e., evaluations at each DOF) at time t^k with input parameter $\boldsymbol{\mu}_{\text{test}}^{(i)}$, respectively. Note that we only present the results of the temperature field. Hence, φ_h and $\widehat{\varphi}_h$ represent T_h and \widehat{T}_h , respectively. From SI-Animation-Example 1, we observe that BT-AE 16 Q provides a reasonable approximation of the temperature field.

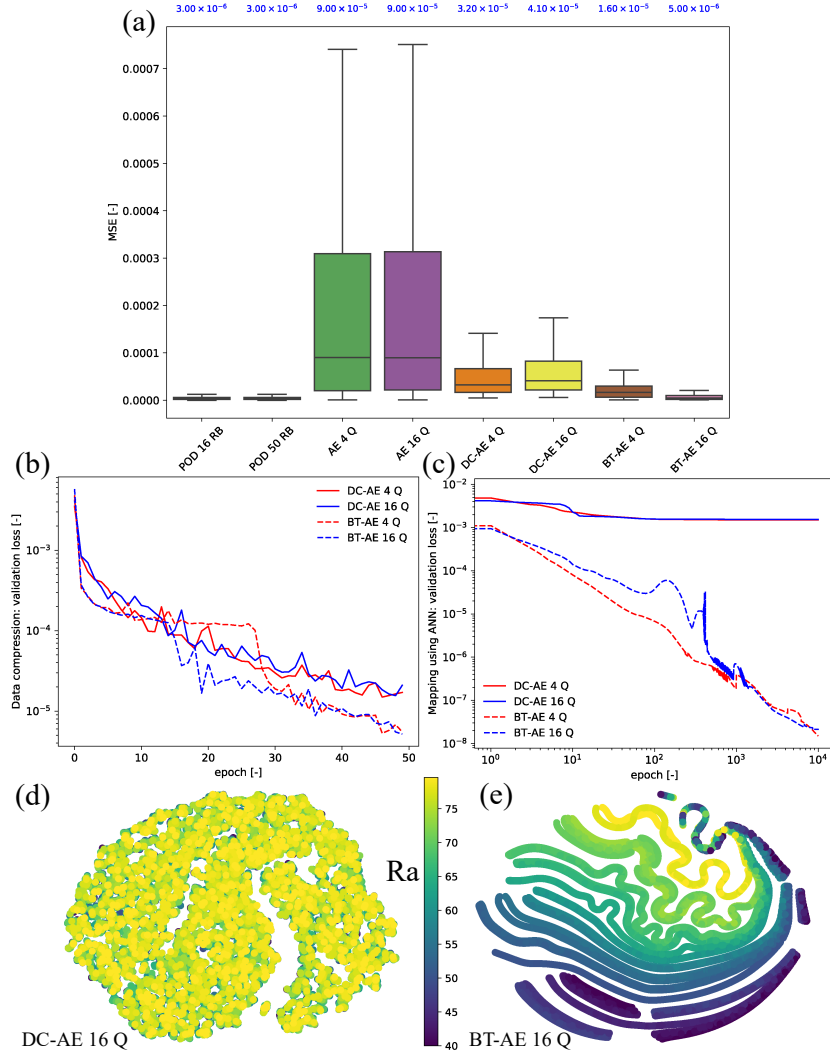


Figure 2. Example 1 - results: (a) mean squared error (MSE) of each model (please refer to Table 2), and blue texts represent a mean value of the box plots - here we show that BT-AE 16 gives performance similar to POD-based approaches, but AE and DC-AE models don't, (b) data compression loss for validation set (Equation (18)), (c) mapping using ANN loss for validation set (Equation (19)), (d) latent space plot of DC-AE 16 Q model, and (e) latent space plot of BT-AE 16 Q model. Latent space plots are constructed using t-Distributed Stochastic Neighbor Embedding (t-SNE). Different colors represent each value of Ra value. We calculate the t-SNE plots using Scikit-Learn package using its default setting and perplexity of 15.

The results of Example 1 is presented in Figure 2. In Figure 2a, The performance of the different models (Table 2) is evaluated with the mean square error ($\text{MSE}_{\varphi}(\cdot, \boldsymbol{\mu}_{\text{test}}^{(i)})$) of the test cases defined as follows

$$\text{MSE}_{\varphi}(\cdot, \boldsymbol{\mu}_{\text{test}}^{(i)}) := \frac{1}{N^t} \sum_{k=0}^{N^t} \left| \varphi_h(\cdot; t^k, \boldsymbol{\mu}_{\text{test}}^{(i)}) - \widehat{\varphi}_h(\cdot; t^k, \boldsymbol{\mu}_{\text{test}}^{(i)}) \right|_{\varphi}^2 \quad (2)$$

where $\text{MSE}_{\varphi}(\cdot, \boldsymbol{\mu}_{\text{test}}^{(i)})$ represents the MSE values of all t for each $\boldsymbol{\mu}_{\text{test}}^{(i)}$. The MSE results show that BT-AE models perform better than AE and DC-AE models. Besides, BT-AE 16 Q delivers similar MSE results to those of the POD models. In contrast to the findings presented in Kadeethum et al.⁴ where the linear compression (POD) outperforms nonlinear compression (AE and DC-AE), BT-AE models in this study could perform similar to the POD models. To be accurate, BT-AE models still underperform, but errors are comparable.

We then investigate how the performance of BT-AE models compares to DC-AE. First, we examine the data compression loss of the validation set (see Equation (18)) which is presented in Figure 2b. From this Figure, the data compression losses of BT-AE models are slightly better than those of the DC-AE models. Subsequently, we illustrate the mapping using ANN loss of the validation set, see Equation (19), in Figure 2c. From Figure 2c, we observe that the mapping losses of the BT-AE models are six orders of magnitude less than those of the DC-AE models. This behavior shows that the BT-AE's latent spaces are easier to be mapped (i.e., ANN loss of the validation set for the BT-AE mapping is much lower than that of the DC-AE.). This speculation is explained by Figures 2d-e, using a t-Distributed Stochastic Neighbor Embedding (t-SNE) plot. From Figure 2d, one could see that all latent variables of DC-AE 16 Q blend (i.e., you cannot differentiate among cases with different Ra values.). The latent variables of the BT-AE 16 Q model, on the other hand, shown in Figure 2e, behave in a much better structure (i.e., we can differentiate among cases with different Ra values.).

Example 2: Elder problem

The Elder problem⁴⁵ is a significantly more complicated and ill-posed problem^{45,46}. High Ra numbers considered in this case may cause the flow instability to be fingering behavior. The domain and boundary conditions are presented in Figure 1b^{4,25,47}. In short, the model domain is heated from the half of the bottom boundary (Figure 1b), and the flow is driven upwards by buoyancy force. We set $\boldsymbol{\mu} = (Ra)$, and its admissible range as [350.0,400.0] (Table 1). Compared to Example 1, this higher range of Ra values affects the minimum and maximum N^t as its range increases to [790, 1010].

The results of Example 2 are presented in Figure 3. From Figure 3a, we observe that all the models using nonlinear compression (AE, DC-AE, and BT-AE) perform better than the linear compression (POD). Furthermore, the BT-AE model accuracy is comparable to that of the DC-AE models. However, the BT-AE model results seem to be insensitive to the number of Q, while the DC-AE model results are affected by the number of Q (i.e., the DC-AE 16 Q and DC-AE 256 Q are more accurate than the DC-AE 4 Q.). We also present the results of the test cases for the BT-AE 16 Q model in the supplemental animation (SI-Animation-Example 2). From these results, we observe that the BT-AE 16 Q model delivers a reasonable approximation of the solution T_h (i.e., \hat{T}_h).

We present the data compression loss of the validation set (Equation (18)) in Figure 3b. In contrast to the ones shown in Figure 2b, the DC-AE models have a slightly lower loss than that of the BT-AE models. We then investigate the ANN mapping loss (see Equation (19)) of the validation set in Figure 3c. Similar to those presented in Figure 2c, the BT-AE models have much lower mapping losses compared to those of the DC-AE models. Among the BT-AE models, BT-AE 256 Q has the highest value of ANN mapping loss, which is expected since it has the highest output dimension (i.e., we are mapping t and $\boldsymbol{\mu}$ to \boldsymbol{z}^Q). Again, we observe a much better structure of the BT-AE 16 Q latent space than the one from DC-AE 16 Q (see Figures 3d-e). To elaborate, the latent variables of the DC-AE 16 Q are overlapped to hinder us from differentiating among each case (different Ra values). The latent variables of the BT-AE, on the contrary, are structured in a way that one can clearly observe different parts that represent different Ra values as shown in Figures 3e.

Model performance of BT-AE models on complex geometries

From Examples 1 and 2, we have observed that the BT-AE models could provide good results while operating on unstructured data. In this section, more challenging geometries which require an unstructured mesh for the FOM are evaluated with BT-AE models only since other methods are not suitable for unstructured mesh problems.

Example 3: Unit cell of micromodel

Example 3 uses a unit cell of micromodel where a central part of honeycomb shape and four corners are impermeable for flow. Still, the heat can conduct through these five subdomains as presented in Figure 1c. Over the past decade, the micromodel has been used to study multiple coupled processes, including flow, reactive transport, bioreaction, and flow instability^{18,19,48-51}. The flow is initiated from an influx at the bottom of the domain. This geometry is more complex than those utilized in Examples 1 and 2 (see Figures 1a-b). The higher temperature at the bottom surface (shown in red) alters a fluid density at the bottom, and subsequently, a buoyancy force drives the flow upwards from the bottom (shown in red) to the top of the domain. Five subdomains contain very low flow conductivity, but they can conduct heat. Again, we set $\boldsymbol{\mu} = (Ra)$ and its range as [350.0,400.0] (Table 1). The range of Ra can also cause flow instability. We use $M = 40$, $M_{\text{validation}}N^t = 10\%$ of MN^t , and $M_{\text{test}} = 10$. We have in total $MN^t = 44354$ training data points.

The summary of the Example 3 results is shown in Figure 4. For all test cases the MSE values over time in Figures 4a-c are in the range of $\approx 1 \times 10^{-5}$. The MSE values tend to decrease over time until the temperature field becomes a steady state. Besides, BT-AE models with different Q values provide approximately similar results (in line with our findings from Examples 1 and 2). The behavior infers that utilizing only a small number of latent spaces; the model can achieve the same level of accuracy as the one with a large number of latent spaces. This behavior is very beneficial because the mapping between parameter space and latent space becomes more manageable. We also present the results of the test cases for the BT-AE 16 Q

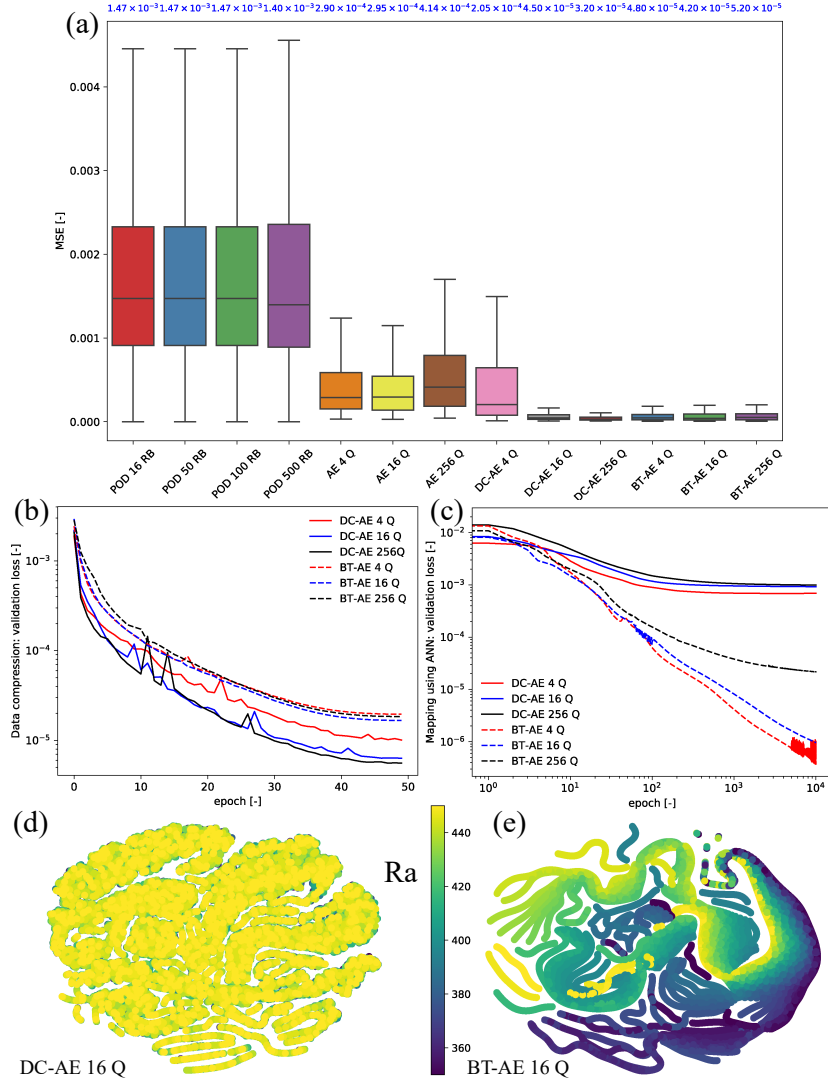


Figure 3. Example 2 - results: (a) mean squared error (MSE) of each model (please refer to Table 2), and blue texts represent a mean value of the box plots - here we show that BT-AE models provide performance similar to DC-AE models, but POD-based approaches and AE models don't, (b) data compression loss for validation set (Equation (18)), (c) mapping using ANN loss for validation set (Equation (19)), (d) latent space plot of DC-AE 16 Q model, and (e) latent space plot of BT-AE 16 Q model. Latent space plots are constructed using t-Distributed Stochastic Neighbor Embedding (t-SNE). Different colors represent each value of Ra value. We calculate the t-SNE plots using Scikit-Learn package using its default setting and perplexity of 15.

model in the supplemental animation (SI-Animation-Example 3). Overall, BT-AE 16 Q delivers a reasonable approximation of the T_h (i.e., DIFF results are low, and the relative error lies within 2 %).

The data compression loss (Equation (18)) is in the range of $\approx 1 \times 10^{-5}$ to 1×10^{-6} (Figure 4d) which is similar to that of Example 1 (Figure 2b), but slightly lower than that of the Example 2 (Figure 3b). The data compression loss seems to be invariant to Q values. We also present the Barlow Twins loss (Equation (14)) in Figure 4e. We observe that the Barlow Twins loss increases with increasing the Q value as in Zbontar et al.⁴⁴. This can be explained that as the Q value grows larger, the cross-correlation matrix $\mathbf{C}^T(t, \boldsymbol{\mu})$ becomes bigger, resulting in more members in Equations (15) and (16). As stated by Zbontar et al.⁴⁴, the absolute value of Equations (15) and (16) is not as important as their trend. To elaborate this, in Figure 4e, all models (different Q values) reach their saturated points around 40 epochs, meaning that the minimization of Equations (15) and (16) is completed.

The mapping of the latent space using ANN loss (Equation (19)) is presented in Figure 4f. Similar to Examples 1 and 2 (Figures 2c and 3c), the mapping loss is in range of $\approx 1 \times 10^{-5}$ to 1×10^{-7} . The higher Q values, the mapping loss grows larger because there are more outputs to map. We present the latent space structure in Figure 4g (only for BT-AE 16 Q). Following the

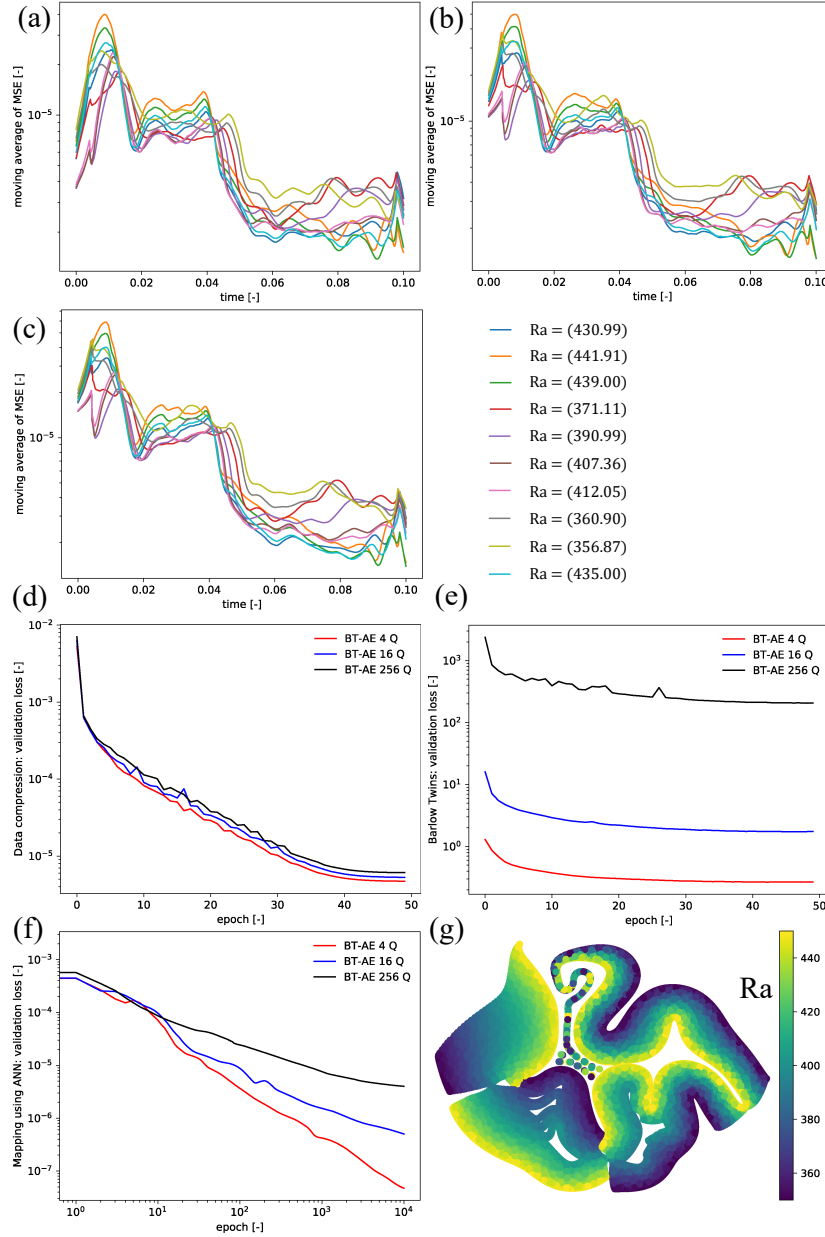


Figure 4. Example 3 results: the moving average (a window size of 50) of mean squared error (MSE) of (a) BT-AE 4 Q, (b) BT-AE 16 Q, (c) BT-AE 256 Q (please refer to Table 2). (d) Data compression loss for validation set (Equation (18)), (e) Barlow Twins loss for validation set (Equation (14)), (f) mapping using ANN loss for validation set (Equation (19)), and (g) latent space plot of BT-AE 16 Q model. Latent space plots are constructed using t-Distributed Stochastic Neighbor Embedding (t-SNE). Different colors represent each value of Ra value. We calculate the t-SNE plots using Scikit-Learn package using its default setting and perplexity of 15.

results shown in Figures 2e and 3e, the latent structure of the BT-AE model has a good structure since we can differentiate among different Ra values. This behavior stems from the fact that the BT losses maximize the information content of the embedding with the latent space through a joint embedding architecture.

Example 4: Modified Hydrocoid with four subdomains

Example 4 uses the hydrocoid problem^{52,53} with the domain geometry shown in Figure 1d. In this example, the domain is subdivided into four subdomains with different Ra values (i.e., $\boldsymbol{\mu} = (Ra_1, Ra_2, Ra_3, Ra_4)$). The range of Ra values is $[350.0, 400.0]$. Similar to the previous examples, this Ra range causes fingering behavior as shown in the supplemental

animation (SI-Animation-Example4). We use $M = 81$, $M_{\text{validation}}N^t = 10\%$ of MN^t , and $M_{\text{test}} = 10$. We have in total $MN^t = 90175$ training data points. We note that as we use $M = 81 = 3^4$ equally spaced samples, for each parameter Ra_i , $i = 1, 2, 3, 4$, we only have three values. As an example, for Ra_1 we only sample $Ra_1 = (350, 400, 450)$ for the training set. The same goes for Ra_2, Ra_3 , and Ra_4 . As a result, training with relatively sparse samples of each parameter Ra_i makes it very challenging to obtain an accurate data-driven framework in general^{1,2}.

Even though this setting is very challenging, we still observe that the BT-AE 16 Q delivers a reasonable approximation of the T_h as seen in the supplemental animation (SI-Animation-Example4). The summary of the Example 4 results is shown in Figure 5. We present the MSE values as a function of time in Figure 5a-c. We can observe that the MSE values for all test cases are in the range of $\approx 1 \times 10^{-1}$ to 1×10^{-5} , which are significantly higher than those of Examples 1, 2, and 3. Moreover, the MSE values generally increase as we approach steady-state solutions, unlike the behaviors shown in Example 3. Again, BT-AE models with different Q provide approximately similar results (in line with our finding from Examples 1, 2, and 3).

The data compression loss (Equation (18)) is in the range of $\approx 1 \times 10^{-2}$ to 1×10^{-4} (Figure 5d), which is significantly higher than that of Examples 1, 2, and 3. This behavior illustrates that this example is the most challenging case for the BT-AE models. The data compression loss is the lowest for $Q = 256$ and the highest for $Q = 4$, but the difference is not critical. As shown in the Barlow Twins loss (Equation (14)) in Figure 5e, the higher values of Q the larger Barlow Twins loss is (as we discussed in the previous example.).

The mapping of the latent space using ANN loss (Equation (19)) is presented in Figure 5f. The mapping loss is in the range of $\approx 1 \times 10^{-4}$ to 1×10^{-5} , which is significantly higher than those of Examples 1, 2, and 3 (see Figures 2c, 3c, and 4f). This behavior also contributes to the higher MSE values of the BT-AE models. We present the latent space structure (only for BT-AE 16 Q) in Figure 5g-h for Ra_1 and Ra_4 , respectively. Since Example 4 has different Ra values in four subdomains, the differentiation of the latent space of individual Ra does not provide good solutions as each latent space of each subdomain might also be interconnected.

Discussion

Recent developments in ML-based data-driven reduced order modeling (DL-ROM or DC-AE in this study)^{3,4} have shown promising results in capturing parametrized solutions of systems of nonlinear equations. These models, however, rely on convolutional operators, which hinders the applicability of these models to complex geometries where an unstructured mesh is required for FOMs, as in Examples 3 and 4. Though we could utilize an autoencoder without convolutional layers, the model could not achieve the same level of accuracy as DL-ROM⁴. Kadeethum et al.⁴ also illustrate that in a specific setting (simple geometry and boundary conditions), a linear compression approach using POD can outperform the DL-ROM model (Example 1). We have demonstrated that the autoencoder model through Barlow Twins self-supervised learning (BT-AE) could achieve the same accuracy as DL-ROM (Example 2 where POD models perform much worse than DL-ROM) by regularizing the latent space or nonlinear manifolds. Besides, it also yields optimal results in the case where the linear compression model outperforms the DL-ROM (Example 1). It means that the BT-AE model excels in all the test cases (Examples 1 and 2) while it still can operate on an unstructured mesh. This behavior has a significant advantage in scientific computing since most realistic problems require unstructured mesh representations. Besides, the BT-AE's performance is insensitive to the number of latent spaces, suggesting that with only a small number of latent spaces, the model can achieve the same level of accuracy as the one with a large number of latent spaces. This behavior is very beneficial because the mapping between parameter space and latent space becomes more manageable.

The computational time used to develop our ROM can be broken down into three primary parts: (1) generation of training data through FOM (the second step in Figure 6), (2) training BT-AE (the third step in Figure 6), and (3) mapping of t and $\boldsymbol{\mu}$ to reduced subspace (the fourth step in Figure 6). Each FOM model (corresponding to each set of $\boldsymbol{\mu}$ or Ra in this work) takes, on average, about two hours on AMD Ryzen Threadripper 3970X (4 threads). We note that our FOM utilizes the adaptive time-stepping; hence, each $\boldsymbol{\mu}^{(i)}$ may require a substantially different computational time. To elaborate, cases that have higher Ra usually have a smaller time-step (N^t becomes larger), and subsequently, they require more time to complete.

The wall time used to train BT-AE is approximately 0.4 hours using a single Quadro RTX 6000. It is noted that this computational cost is much cheaper than that of the DC-AE model, taking around four to six hours⁴. This is because DC-AE relies on convolutional layers, dropout, and batch normalization, which require much higher computational resources. The BT-AE, on the other hand, utilizes only a plain autoencoder. The BT-AE model is also cheaper than the POD model. However, we note that this may not be a fair comparison as we perform POD and BT-AE using different machines (i.e., our POD framework only works on CPU, but our BT-AE is trained using GPU). Please refer to Kadeethum et al.⁴ for detailed wall time comparisons among POD and DC-AE models. The mapping of t and $\boldsymbol{\mu}$ to reduced subspace through artificial neural networks (ANN) takes around half an hour to one hour using a single Quadro RTX 6000. As mentioned in the Methodology section, we do not terminate the training of both BT-AE and mapping of t and $\boldsymbol{\mu}$ to reduced subspace through ANN early, but rather use the model with the best validation loss through the final epochs. For example, we train for 50 epochs, but the model that offers the

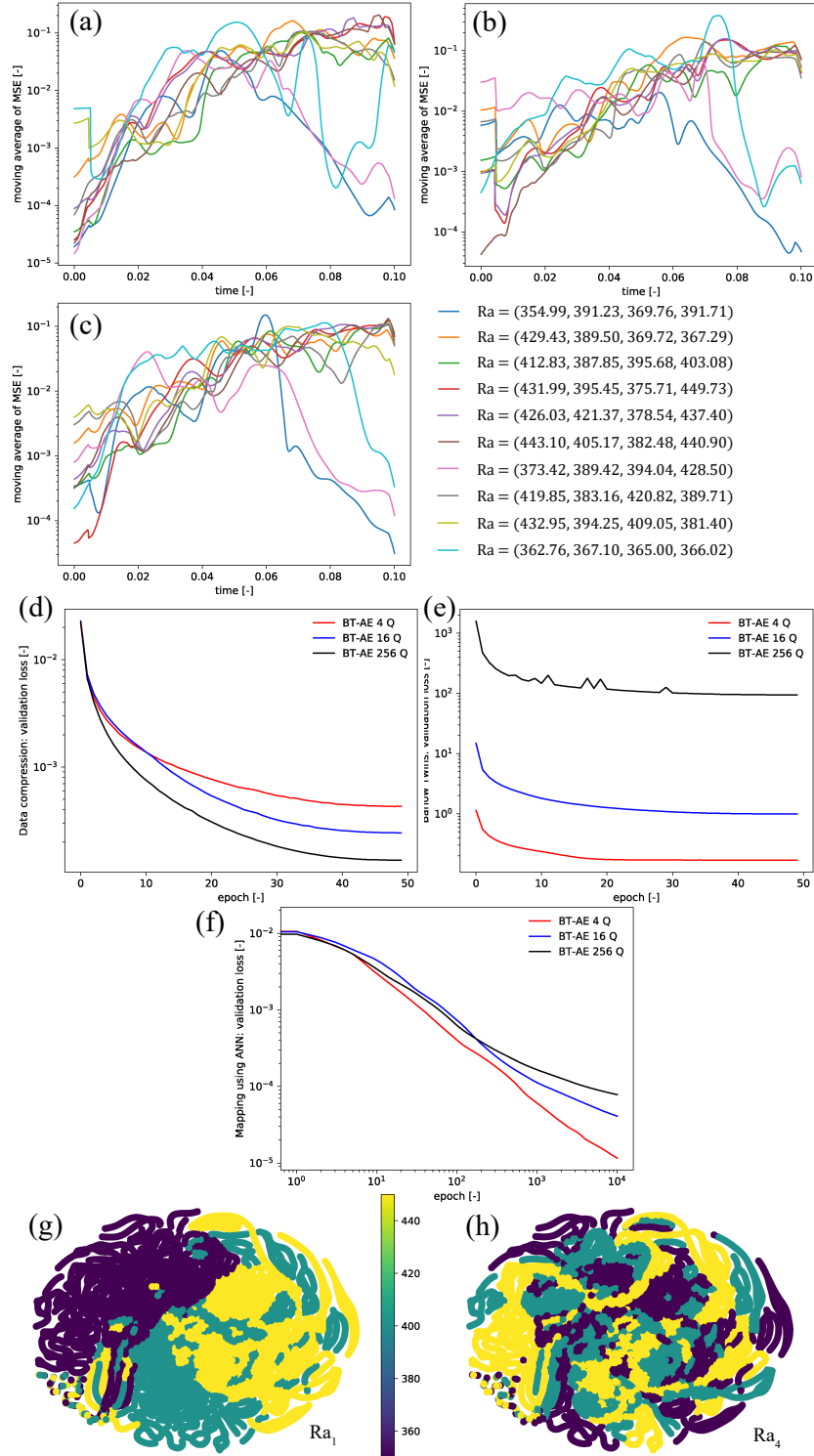


Figure 5. Example 4 results: the moving average (a window size of 50) of mean squared error (MSE) of (a) BT-AE 4 Q, (b) BT-AE 16 Q, (c) BT-AE 256 Q (please refer to Table 2). (d) Data compression loss for validation set (Equation (18)), (e) Barlow Twins loss for validation set (Equation (14)), (f) mapping using ANN loss for validation set (Equation (19)), and latent space plot of BT-AE 16 Q model for (g) Ra_1 and (h) Ra_4 . Latent space plots are constructed using t-Distributed Stochastic Neighbor Embedding (t-SNE). Different colors represent each value of Ra value. We calculate the t-SNE plots using Scikit-Learn package using its default setting and perplexity of 15.

best validation loss might be the model at 20 epochs. However, the training time we report here is for 50 epochs. Thus, our training time provided here is considered conservative.

The main advantage of ROM is the gain towards the computational time during the prediction or the online phase. Once the ROM is trained, it could be used speedily. One inquiry - a pair of t^k and $\boldsymbol{\mu}^{(i)}$ takes only several milliseconds. Hence, one typically enjoys an inexpensive prediction compared to FOM. To elaborate, one FOM simulation, i.e., $\boldsymbol{\mu}^{(i)}$ for all t , takes two hours, as mentioned previously, but one ROM simulation would take approximately one second for an evaluation of the quantities of interest at all timestamps used in FOM, $0 =: t^0 < t^1 < \dots < t^N := \tau$. In practice, however, the ROM is not bound by CFL condition; hence, it can deliver the quantities of interest at any specific timestamps without computing at intermediate timestamps. Assuming we only require our quantities of interest at the final time, for Example 2, our ROM could provide a speed-up of 7×10^6 . In short, our framework could provide a speed-up of 7×10^3 to 7×10^6 . We want to note that for the same data, the computational cost of POD is much cheaper than that of neural network training. Thus, even though the BT-AE can achieve comparable accuracy to the POD for the problems with fast decaying Kolmogorov's width, we still might prefer POD to neural network because of POD's simplicity in the training phase.

Our model is developed upon the data-driven paradigm, which is applicable to any FOM. Besides, it could be trained using data produced by FOM, on-site measurements, experimental data, or a combination among them. This characteristic provides flexibility, which intrusive approaches could not provide. The data-driven model, though, is usually hungry for training samples. We have illustrated that as the dimensionality of our parameter space grows, the model requires more training samples, or it will suffer by losing its accuracy significantly as in Example 4 compared to accurate prediction in Example 3. We speculate that an adaptive sampling technique^{33,54,55}, incorporating physical information^{56,57}, or including multimodal unsupervised training⁵⁸ might provide a resolution to this issue in the future work. Besides, as the parameter space grows, the entangle among parameters (correlation) could also cause our model's accuracy to deteriorate (e.g., Example 4).

Methodology

A graphical summary of our procedure is presented in Figure 6: the computations are divided into an offline phase for the ROM construction, which we will show through four consecutive main steps and (single-step) online stage for the ROM evaluation.

The first step of the offline stage represents an initialization of a training set ($\boldsymbol{\mu}$), validation set ($\boldsymbol{\mu}_{\text{validation}}$), and test set ($\boldsymbol{\mu}_{\text{test}}$) of parameters used to train, validate, and test the framework, of cardinality $M, M_{\text{validation}}, M_{\text{test}}$. For the rest of sections we will discuss only $\boldsymbol{\mu}$. The same analogy goes for $\boldsymbol{\mu}_{\text{validation}}$ and $\boldsymbol{\mu}_{\text{test}}$. Let $\mathbb{P} \subset \mathbb{R}^P, P \in \mathbb{N}$, be a compact set representing the range of variation of the parameters $\boldsymbol{\mu} \in \mathbb{P}$. For the sake of notation we denote by $\mu_p, p = 1, \dots, P$, the p -th component of $\boldsymbol{\mu}$. To explore the parametric dependence of the phenomena, we define a discrete training set of M parameter instances. Each parameter instance in the training set will be indicated with the notation $\boldsymbol{\mu}^{(i)}$, for $i = 1, \dots, M$. Thus, the p -th component of the i -th parameter instance in the training set is denoted by $\mu_p^{(i)}$ in the following. The choice of the value of M , as well as the sampling procedure from the range \mathbb{P} , is typically user- and problem-dependent. In this work, we use an equispaced distribution for the training set as done in^{4,41}.

In the second step, we query the FOM, based on the finite element solver proposed and made publicly available in Kadeethum et al.^{4,24}, for each parameter $\boldsymbol{\mu}$ in the training set. In short, we are interested in gravity driven flow in porous media, and here we briefly describe all the equations used in this study: (1) mass balance and (2) heat advection-diffusion equations. Let $\Omega \subset \mathbb{R}^d$ ($d \in \{1, 2, 3\}$) denote the computational domain and $\partial\Omega$ denote the boundary. \mathbf{X}^* are spatial coordinates in Ω (e.g., $\mathbf{X}^* = [x^*, y^*]$ when $d = 2$, which we will focus on throughout this study). The time domain is denoted by $\mathbb{T} = (0, \tau]$ with $\tau > 0$ (i.e., τ is the final time). Primary variables used in this paper are $\mathbf{u}^*(\cdot, t^*) : \Omega \times \mathbb{T} \rightarrow \mathbb{R}^d$, which is a vector-valued Darcy velocity (m/s), $p^*(\cdot, t^*) : \Omega \times \mathbb{T} \rightarrow \mathbb{R}^d$, which is a scalar-valued fluid pressure (Pa), and $T^*(\cdot, t^*) : \Omega \times \mathbb{T} \rightarrow \mathbb{R}^d$, which is a scalar-valued fluid temperature (C). Time is denoted as t^* (s).

Following Joseph⁵⁹, the Boussinesq approximation to the mass balance equations results in the density difference only appearing in the buoyancy term. The mass balance equation reads

$$\mathbf{u}^* + \boldsymbol{\kappa}(\nabla p^* + \mathbf{y}(\rho - \rho_0)g) = 0, \quad (3)$$

and

$$\nabla \cdot \mathbf{u}^* = 0 \quad (4)$$

where $\boldsymbol{\kappa} = \mathbf{k}/\mu_f$ is the porous medium conductivity, \mathbf{k} is the matrix permeability tensor, μ_f is the fluid viscosity, \mathbf{y} is a unit vector in the direction of gravitational force, g is the constant acceleration due to gravity, ρ and ρ_0 are the fluid density at

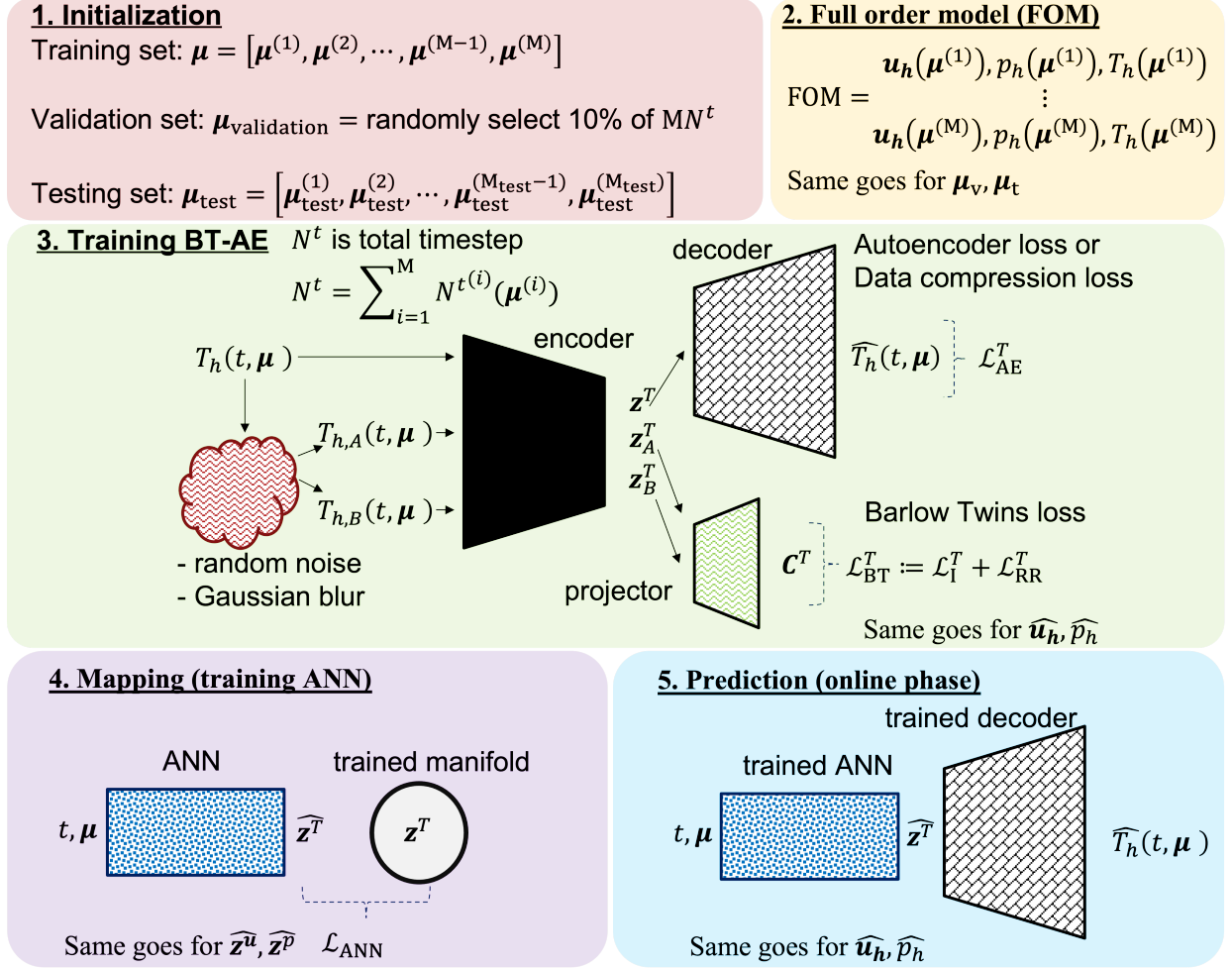


Figure 6. The summary of procedures taken to establish the proposed BT-AE.

current and initial states, respectively. We assume that ρ is a linear function of T ^{25,60}

$$\rho = \rho_0 (1 - \alpha (T^* - T_0^*)), \quad (5)$$

where α is the thermal expansion coefficient, and T_0^* is the reference fluid temperature. We note that Equation (5) is the simplest approximation, and one may easily adapt the proposed method when employing a more complex relationship provided in⁶¹. The heat advection-diffusion equation defined as

$$\gamma \frac{\partial T^*}{\partial t^*} + \mathbf{u}^* \cdot \nabla T^* - K \nabla^2 T^* - f_c^* = 0. \quad (6)$$

Here, γ is the ratio between the porous medium heat capacity and the fluid heat capacity, K is the effective thermal conductivity, and f_c^* is a sink/source. We follow Nield and Bejan¹⁷ and define dimensionless variables as follows

$$\mathbf{X} := \frac{1}{H} \mathbf{X}^*, \quad t := \frac{\kappa}{\mu \gamma H^2} t^*, \quad p := \frac{\kappa}{K} p^*, \quad \mathbf{u} := \frac{H}{K} \mathbf{u}^*, \quad T := \frac{T^* - T_0^*}{\Delta T^*}, \quad f_c := \frac{t^*}{\Delta T^*} f_c^*, \quad (7)$$

where H is the dimensional layer depth, and ΔT^* is the temperature difference between two boundary layers. From these

dimensionless variables, we could rewrite our Equations (3) and (4) as

$$\begin{aligned}
\mathbf{u} + \nabla p - \mathbf{y} \text{Ra} T &= 0, \quad \text{in } \Omega \times \mathbb{T}, \\
\nabla \cdot \mathbf{u} &= 0, \quad \text{in } \Omega \times \mathbb{T}, \\
p &= p_D \quad \text{on } \partial\Omega_p \times \mathbb{T}, \\
\mathbf{u} \cdot \mathbf{n} &= q_D \quad \text{on } \partial\Omega_q \times \mathbb{T}, \\
p &= p_0 \quad \text{in } \Omega \text{ at } t = 0,
\end{aligned} \tag{8}$$

where $\partial\Omega_p$ and $\partial\Omega_q$ are the pressure and flux boundaries (i.e., Dirichlet and Neumann boundary conditions), respectively. Here, Ra is the Rayleigh number

$$\text{Ra} := \frac{g\alpha\kappa\Delta T^* H}{K}. \tag{9}$$

We then write Equation (6) in dimensionless form as follows

$$\begin{aligned}
\frac{\partial T}{\partial t} + \mathbf{u} \cdot \nabla T - \nabla^2 T - f_c &= 0, \quad \text{in } \Omega \times (0, \mathbb{T}], \\
T &= T_D \quad \text{on } \partial\Omega_T \times (0, \mathbb{T}], \\
(-\mathbf{u}T + \nabla T) \cdot \mathbf{n} &= T_{\text{in}} \mathbf{u} \cdot \mathbf{n} \quad \text{on } \partial\Omega_{\text{in}} \times (0, \mathbb{T}], \\
\nabla T \cdot \mathbf{n} &= 0 \quad \text{on } \partial\Omega_{\text{out}} \times (0, \mathbb{T}], \\
T &= T_0 \quad \text{in } \Omega \text{ at } t = 0,
\end{aligned} \tag{10}$$

where $\partial\Omega_T$ is temperature boundary (Dirichlet boundary condition), $\partial\Omega_{\text{in}}$ and $\partial\Omega_{\text{out}}$ denote inflow and outflow boundaries, respectively, which are defined as

$$\partial\Omega_{\text{in}} := \{\mathbf{X} \in \partial\Omega : \mathbf{u} \cdot \mathbf{n} < 0\} \quad \text{and} \quad \partial\Omega_{\text{out}} := \{\mathbf{X} \in \partial\Omega : \mathbf{u} \cdot \mathbf{n} \geq 0\}. \tag{11}$$

The detail of discretization could be found in Kadeethum et al.^{4,24}, and the FOM source codes are provided in Kadeethum et al.²⁴. After the second step, we have M snapshots of FOM results associated with the different parametric configurations in $\boldsymbol{\mu}$. Since the problem formulation is time-dependent, the output of the FOM solver for each parameter instance $\boldsymbol{\mu}^{(i)}$ collects the time series representing the time evolution of the primary variables for each time-step t . Thus, each snapshot contains approximations of the primary variables (\mathbf{u}_h , p_h , and T_h) at each time-step of the partition of the time domain \mathbb{T} . Therefore, based on the training set cardinality M and the number N^t of time-steps, we have a total of $N^t M$ training data to be employed in the subsequent steps. We note that as our finite element solver utilizes an adaptive time-stepping^{4,24}, each snapshot may have a different number of time-steps N^t , i.e. $N^t = N^t(\boldsymbol{\mu})$.

The third step aims to compress the information provided by the training snapshots provided by the second step. Kadeethum et al.⁴ provide detailed derivations and comparisons between linear and nonlinear compression. Especially the convolutional layers, in their classical form, could not deal with an unstructured data structure (unstructured mesh), which is very common in scientific computing or, more specifically, finite element analysis. Hence, our goal is to develop a nonlinear compression that (1) consistently outperforms (or at least delivers similar accuracy) the linear compression and (2) is compatible with an unstructured data structure.

To achieve this goal, we propose a nonlinear compression utilizing feedforward layers in combination with self-supervised learning (SSL) of Barlow Twins (BT) (Figure 6). The BT for redundancy reduction is proposed by Zbontar et al.⁴⁴. It operates on a joint embedding of noisy images by producing two distorted images from an original one through a series of random cropping, resizing, horizontal flipping, color jittering, converting to grayscale, Gaussian blurring, and solarization. Since we do not operate on structured data (image) but unstructured data produced by finite element solver, we only employ random noise and Gaussian blur operations to produce our noisy data set, see Figure 6.

Let $z_1^{\mathbf{u}}, \dots, z_Q^{\mathbf{u}}$, z_1^p, \dots, z_Q^p , and z_1^T, \dots, z_Q^T be the nonlinear manifolds of the \mathbf{u}_h , p_h , and T_h , respectively. For the sake of compactness, we will only discuss primary variable T_h . The same procedure holds for \mathbf{u}_h and p_h . Our goal is to achieve $Q \ll MN^t$ where MN^t is the total training data, which implies that our nonlinear manifolds could represent our training data using much lower dimension. We employ a vanilla AE (using only feedforward layers) that is regularized by Barlow Twins

Algorithm 1 Training autoencoder (AE) with Barlow Twins (BT) regularization

```
# Integrate BT into AE architecture to regularize AE's latent spaces  $\mathbf{z}^T$ 
###
# Training data  $T_h$  and distorted data  $T_{h,A}, T_{h,B}$  are input of encoder
# latent spaces  $\mathbf{z}^T, \mathbf{z}_A^T,$  and  $\mathbf{z}_B^T$  are output encoder
###
# latent space  $\mathbf{z}^T$  is output of decoder
# Approximation of  $T_h$ , i.e.,  $\hat{T}_h$  is output of decoder
###
# latent spaces  $\mathbf{z}_A^T$  and  $\mathbf{z}_B^T$  are input of projector
# cross-correlation matrix  $\mathbf{C}^T$  is output of projector
###
1: Initialize (or load pre-trained models) encoder, decoder, and projector           ▷ size of latent space Q has to be specified.
2: Initialize (or load pre-trained optimizers) two optimizers for AE and BT.
3: Load training set  $\boldsymbol{\mu}$                                                          ▷ the total training data is  $MN^I$ 
4: Randomly select 10% of  $MN^I$  for validation set  $\boldsymbol{\mu}_{\text{validation}}$              ▷ the total training data becomes 90% of  $MN^I$ 
5: Add random noise                                                                    ▷ see Equation (12)
6: Add Gaussian blur                                                                    ▷ see Equation (13)
7: From step 4 and 5, we obtain  $T_{h,A}(t, \boldsymbol{\mu})$  and  $T_{h,B}(t, \boldsymbol{\mu})$  from  $T(t, \boldsymbol{\mu})$ 
8: for each epoch do
9:   Outer loop: training BT                                                         ▷ Batch size  $\mathbf{B}_{\text{outer}} = 512$ 
10:  for each  $\mathbf{B}_{\text{outer},i} \in \mathbf{B}_{\text{outer}}$  do
11:     $\mathbf{z}_{h,A}^T(t, \boldsymbol{\mu}) = \text{encoder}(T_{h,A}(t, \boldsymbol{\mu}))$ 
12:     $\mathbf{z}_{h,B}^T(t, \boldsymbol{\mu}) = \text{encoder}(T_{h,B}(t, \boldsymbol{\mu}))$ 
13:     $\mathbf{C}^T(t, \boldsymbol{\mu}) = \text{projector}(\mathbf{z}_{h,A}^T(t, \boldsymbol{\mu}), \mathbf{z}_{h,B}^T(t, \boldsymbol{\mu}))$ 
14:    Calculate BT loss  $\mathcal{L}_{\text{BT}}^T$                                                          ▷ see Equation (14)
15:    Back-propagation of BT loss w.r.t. each encoder ( $\mathbf{W}, \mathbf{b}$ ) and projector ( $\mathbf{W}, \mathbf{b}$ )
16:    Update encoder ( $\mathbf{W}, \mathbf{b}$ ) and projector ( $\mathbf{W}, \mathbf{b}$ ) using BT optimizer
17:    Update learning rate  $\eta_c$  of BT optimizer                                         ▷ see Equation (17)
18:    Inner loop: training AE                                                         ▷ Batch size  $\mathbf{B}_{\text{inner}} = 32$ 
19:    for each  $\mathbf{B}_{\text{inner},i} \in \mathbf{B}_{\text{inner}}$  do
20:       $\mathbf{z}^T(t, \boldsymbol{\mu}) = \text{encoder}(T_h(t, \boldsymbol{\mu}))$ 
21:       $\hat{T}_h(t, \boldsymbol{\mu}) = \text{decoder}(\mathbf{z}^T(t, \boldsymbol{\mu}))$ 
22:      Calculate AE loss  $\mathcal{L}_{\text{AE}}^T$  (data compression loss)                             ▷ see Equation (18)
23:      Back-propagation of AE loss w.r.t. each encoder ( $\mathbf{W}, \mathbf{b}$ ) and decoder ( $\mathbf{W}, \mathbf{b}$ )
24:      Update encoder ( $\mathbf{W}, \mathbf{b}$ ) and decoder ( $\mathbf{W}, \mathbf{b}$ ) using AE optimizer
25:      Update learning rate  $\eta_c$  of AE optimizer                                         ▷ see Equation (17)
26:    end for
27:  end for
28: end for
```

It is noted that, we here only discuss primary variable T_h for the sake of compactness. The same procedures are hold for \mathbf{u}_h and p_h . Moreover, this algorithm only reflects the third step in Figure 6.

SSL to obtain $\mathbf{z}^T = [z_1^T, \dots, z_Q^T]$. We do not use any batch normalization or dropout. The summary of the training process is presented in Algorithm 1. We provide the detailed implementation in <https://github.com/sandialabs>.

In short, during the training phase, our BT-AE model is composed of one encoder, one decoder, and one projector. The training entails two sub-tasks; the first is BT (encoder and projector), which takes place in the outer loop. The second sub-task is responsible for the training of AE (encoder and decoder), which takes place inside the inner loop. The main reasons for this procedure are two folds. The first reason is Zbontar et al.⁴⁴ states that the BT works better with large batch sizes. The AE, however, generally requires a small batch size^{62,63}. Our previous numerical experiments based on DC-AE⁴ also align with this statement. Consequently, we set our batch size of the outer loop as $\mathbf{B}_{\text{outer}} = 512$, and the batch size of the inner loop as $\mathbf{B}_{\text{inner}} = 32$

Prior to the training, we distort our training set (i.e., creating $T_{h,A}(t, \boldsymbol{\mu})$ and $T_{h,B}(t, \boldsymbol{\mu})$ from $T(t, \boldsymbol{\mu})$) through a series of two

operations. First, add random noise is added as follows

$$\widetilde{T}_{h,A}(t, \boldsymbol{\mu}), \widetilde{T}_{h,B}(t, \boldsymbol{\mu}) = T(t, \boldsymbol{\mu}) + \varepsilon \text{SD}(T(t, \boldsymbol{\mu})) \mathcal{G}(0, 1) \quad (12)$$

where $\widetilde{T}_{h,A}(t, \boldsymbol{\mu}), \widetilde{T}_{h,B}(t, \boldsymbol{\mu})$ are intermediate distorted input data. The constant ε , which is set to 0.1, determines the noise level as it is multiplied with the standard deviation of the input field. $\mathcal{G}(0, 1)$ is a random value which is sampled from the standard normal distribution with mean and standard deviation of zero and one, respectively.

Subsequently, we pass $\widetilde{T}_{h,A}(t, \boldsymbol{\mu}), \widetilde{T}_{h,B}(t, \boldsymbol{\mu})$ through Gaussian blur operation, which reads

$$T_{h,A}(t, \boldsymbol{\mu}), T_{h,B}(t, \boldsymbol{\mu}) = \frac{1}{\sqrt{2\pi \text{SD}(\widetilde{T}_{h,A}(t, \boldsymbol{\mu}), \widetilde{T}_{h,B}(t, \boldsymbol{\mu}))^2}} \exp\left(-\frac{\widetilde{T}_{h,A}(t, \boldsymbol{\mu}), \widetilde{T}_{h,B}(t, \boldsymbol{\mu})^2}{2 \text{SD}(\widetilde{T}_{h,A}(t, \boldsymbol{\mu}), \widetilde{T}_{h,B}(t, \boldsymbol{\mu}))^2}\right) \quad (13)$$

to obtain $T_{h,A}(t, \boldsymbol{\mu})$ and $T_{h,B}(t, \boldsymbol{\mu})$.

We use a number of the epoch of 50, see Algorithm 1. The outer loop works as follows: training BT begins with passing $T_{h,A}(t, \boldsymbol{\mu})$ and $T_{h,B}(t, \boldsymbol{\mu})$ to the encoder (it is noted we have only one encoder) resulting in $\mathbf{z}_A^T(t, \boldsymbol{\mu})$ and $\mathbf{z}_B^T(t, \boldsymbol{\mu})$. We then use $\mathbf{z}_A^T(t, \boldsymbol{\mu})$ and $\mathbf{z}_B^T(t, \boldsymbol{\mu})$ as input to the projector resulting in cross-correlation matrix $\mathbf{C}^T(t, \boldsymbol{\mu})$. $\mathbf{C}^T(t, \boldsymbol{\mu})$ is a square matrix with the dimensionality of the projector's output, and its values range between -1, perfect anti-correlation, and 1, perfect correlation.

The Barlow Twins loss $\mathcal{L}_{\text{BT}}^T$ (BT loss) is then calculated using

$$\mathcal{L}_{\text{BT}}^T := \mathcal{L}_I^T + \mathcal{L}_{\text{RR}}^T \quad (14)$$

where

$$\mathcal{L}_I^T := \sum_i (1 - \mathbf{C}_{ii}^T(t, \boldsymbol{\mu}))^2, \quad (15)$$

and

$$\mathcal{L}_{\text{RR}}^T := \lambda \sum_i \sum_{j \neq i} \mathbf{C}_{ij}^T(t, \boldsymbol{\mu})^2. \quad (16)$$

where $\mathbf{C}_{ii}^T(t, \boldsymbol{\mu})$ denotes the i -th diagonal entry of $\mathbf{C}^T(t, \boldsymbol{\mu})$, λ is a positive constant, which is set to 5×10^{-3} as recommended by Zbontar et al. (2021)⁴⁴, and \mathbf{C}_{ij}^T are off-diagonal entries of \mathbf{C}^T . In short, we train our BT part by trying to force \mathcal{L}_I^T to 1, but $\mathcal{L}_{\text{RR}}^T$ to 0 resulting in teaching the encoder and projector learn how to get rid off noise from the distorted data, $T_{h,A}(t, \boldsymbol{\mu})$ and $T_{h,B}(t, \boldsymbol{\mu})$, and construct a representation that conserves as much $T(t, \boldsymbol{\mu})$ information as possible.

Here, we follow the training procedures used by Kadeethum et al.^{4,64}. We use the ADAM algorithm⁶⁵ to adjust learnable parameters of encoder(W and b) and projector(W and b). The learning rate (η) is calculated as⁶⁶

$$\eta_c = \eta_{\min} + \frac{1}{2} (\eta_{\max} - \eta_{\min}) \left(1 + \cos\left(\frac{\text{step}_c}{\text{step}_f} \pi\right)\right) \quad (17)$$

where η_c is a learning rate at step step_c , η_{\min} is the minimum learning rate, which is set as 1×10^{-16} , η_{\max} is the maximum or initial learning rate, which is selected as 1×10^{-4} , step_c is the current step, and step_f is the final step. We note that each step refers to each time we perform back-propagation, including updating both encoder and projector's parameters.

The inner loop is as follows: training AE starts with obtaining $\mathbf{z}^T(t, \boldsymbol{\mu})$ by passing $T_h(t, \boldsymbol{\mu})$ to the encoder. We then use $\mathbf{z}^T(t, \boldsymbol{\mu})$ to reconstruct $\widehat{T}_h(t, \boldsymbol{\mu})$ through the decoder. Subsequently, we calculate our data compression loss or AE loss ($\mathcal{L}_{\text{AE}}^T$) using

$$\mathcal{L}_{\text{AE}}^T := \text{MSE}^T = \frac{1}{MN^t} \sum_{i=1}^M \sum_{k=0}^{N^t} \left| \widehat{T}_h(t^k, \boldsymbol{\mu}^{(i)}) - T_h(t^k, \boldsymbol{\mu}^{(i)}) \right|^2. \quad (18)$$

Similar to the training of BT, we use ADAM to adjust learnable parameters of encoder(W and b) and decoder(W and b) according the gradient of Equation (18). The η_c is adjusted by Equation (17). In contrast to the training of BT, we use $\eta_{\min} = 1 \times 10^{-16}$, and $\eta_{\max} = 1 \times 10^{-5}$.

Following the training of the BT-AE, we now establish the manifold $\mathbf{z}^T(t, \boldsymbol{\mu})$, $\forall t \in \mathbb{T}$ and $\forall \boldsymbol{\mu} \in \mathbb{P}$ during the fourth step shown in Figure 6. The data available for this task are the pairs $(t, \boldsymbol{\mu})$ and $\mathbf{z}^T(t, \boldsymbol{\mu})$ in the training set. We achieve this through the training of artificial neural networks (ANN). Following Kadeethum et al.^{4,41}, our ANN has five hidden layers, and each layer has seven neurons. We use tanh as our activation function. Here, we use a mean squared error ($\text{MSE}^{\mathbf{z}^T}$) as the metric of our network loss function, defined as follows

$$\mathcal{L}_{\text{ANN}}^T := \text{MSE}^{\mathbf{z}^T} = \frac{1}{MN^t} \sum_{i=1}^M \sum_{k=0}^{N^t} \left| \hat{\mathbf{z}}^T(t^k, \boldsymbol{\mu}^{(i)}) - \mathbf{z}^T(t^k, \boldsymbol{\mu}^{(i)}) \right|^2. \quad (19)$$

To minimize Equation (19), we use the ADAM algorithm to adjust each neuron \mathbf{W} and \mathbf{b} , a batch size of 32, a learning rate of 0.001, a number of epoch of 10,000, and we normalize both our input $(t, \boldsymbol{\mu})$ and output (\mathbf{z}^T) to $[0, 1]$. To prevent our networks from overfitting behavior, we follow early stopping and generalized cross-validation criteria^{2,67,68}. Note that instead of literally stopping our training cycle, we only save the set of trained weight and bias to be used in the online phase when the current validation loss is lower than the lowest validation from all the previous training cycle.

During the online phase (the fifth step shown in Figure 6), we utilize the trained ANN and the trained decoder to approximate $\hat{T}_h(\cdot; t, \boldsymbol{\mu})$ for each inquiry (i.e., a pair of $(t, \boldsymbol{\mu})$) through

$$\hat{\mathbf{z}}^T(\cdot; t, \boldsymbol{\mu}) = \text{ANN}(t, \boldsymbol{\mu}), \quad (20)$$

and, subsequently,

$$\hat{T}_h(\cdot; t, \boldsymbol{\mu}) = \text{decoder}\left(\hat{\mathbf{z}}^T(\cdot; t, \boldsymbol{\mu})\right). \quad (21)$$

References

1. Hesthaven, J., Rozza, G. & Stamm, B. Certified reduced basis methods for parametrized partial differential equations (Springer, 2016).
2. Hesthaven, J. & Ubbiali, S. Non-intrusive reduced order modeling of nonlinear problems using neural networks. J. Comput. Phys. **363**, 55–78 (2018).
3. Fresca, S., Dede, L. & Manzoni, A. A comprehensive deep learning-based approach to reduced order modeling of nonlinear time-dependent parametrized pdes. J. Sci. Comput. **87**, 1–36 (2021).
4. Kadeethum, T. et al. Non-intrusive reduced order modeling of natural convection in porous media using convolutional autoencoders: comparison with linear subspace techniques. Adv. Water Resour. 104098 (2022).
5. Ahmed, S., San, O., Rasheed, A. & Iliescu, T. Nonlinear proper orthogonal decomposition for convection-dominated flows. Phys. Fluids **33**, 121702 (2021).
6. Phillips, T., Heaney, C., Smith, P. & Pain, C. An autoencoder-based reduced-order model for eigenvalue problems with application to neutron diffusion. arXiv preprint arXiv:2008.10532 (2020).
7. Kim, Y., Choi, Y., Widemann, D. & Zohdi, T. A fast and accurate physics-informed neural network reduced order model with shallow masked autoencoder. J. Comput. Phys. 110841 (2021).
8. Kim, Y., Choi, Y., Widemann, D. & Zohdi, T. Efficient nonlinear manifold reduced order model. arXiv preprint arXiv:2011.07727 (2020).
9. Chatterjee, A. An introduction to the proper orthogonal decomposition. Curr. science 808–817 (2000).
10. Willcox, K. & Peraire, J. Balanced model reduction via the proper orthogonal decomposition. AIAA journal **40**, 2323–2330 (2002).
11. Choi, Y., Coombs, D. & Anderson, R. SNS: a solution-based nonlinear subspace method for time-dependent model order reduction. SIAM J. on Sci. Comput. **42**, A1116–A1146 (2020).
12. Kim, Y., Wang, K. & Choi, Y. Efficient space–time reduced order model for linear dynamical systems in python using less than 120 lines of code. Mathematics **9**, 1690 (2021).

13. Taron, J. & Elsworth, D. Thermal-hydrologic-mechanical-chemical processes in the evolution of engineered geothermal reservoirs. *Int. J. Rock Mech. Min. Sci.* **46**, 855–864 (2009).
14. Nick, H., Raouf, A., Centler, F., Thullner, M. & Regnier, P. Reactive dispersive contaminant transport in coastal aquifers: numerical simulation of a reactive Henry problem. *J. contaminant hydrology* **145**, 90–104 (2013).
15. Zheng, C. & Bennett, G. *Applied contaminant transport modeling*, vol. 2 (Wiley-Interscience New York, 2002).
16. Rutqvist, J. et al. A numerical study of THM effects on the near-field safety of a hypothetical nuclear waste repository—BMT1 of the DECOVALEX III project. part 3: Effects of THM coupling in sparsely fractured rocks. *Int. J. Rock Mech. Min. Sci.* **42**, 745–755 (2005).
17. Nield, D. & Bejan, A. *Convection in porous media*, vol. 3 (Springer, 2006).
18. Davison, S. M., Yoon, H. & Martinez, M. J. Pore scale analysis of the impact of mixing-induced reaction dependent viscosity variations. *Adv. water resources* **38**, 70–80 (2012).
19. Park, S. W., Lee, J., Yoon, H. & Shin, S. Microfluidic investigation of salinity-induced oil recovery in porous media during chemical flooding. *Energy & Fuels* **35**, 4885–4892 (2021).
20. Hassanzadeh, H., Pooladi-Darvish, M. & Keith, D. Scaling behavior of convective mixing, with application to geological storage of CO₂. *AIChE journal* **53**, 1121–1131 (2007).
21. Neufeld, J. et al. Convective dissolution of carbon dioxide in saline aquifers. *Geophys. research letters* **37** (2010).
22. Altman, S. J. et al. Chemical and hydrodynamic mechanisms for long-term geological carbon storage. *The J. Phys. Chem. C* **118**, 15103–15113 (2014).
23. Kadeethum, T., Lee, S. & Nick, H. Finite element solvers for Biot's poroelasticity equations in porous media. *Math. Geosci.* **52**, 977–1015 (2020).
24. Kadeethum, T., Lee, S., Ballarin, F., Choo, J. & Nick, H. A locally conservative mixed finite element framework for coupled hydro-mechanical-chemical processes in heterogeneous porous media. *Comput. & Geosci.* 104774 (2021).
25. Zhang, C., Zarrouk, S. & Archer, R. A mixed finite element solver for natural convection in porous media using automated solution techniques. *Comput. & Geosci.* **96**, 181–192 (2016).
26. Hosseini, N., Bajalan, Z. & Khoei, A. Numerical modeling of density-driven solute transport in fractured porous media with the extended finite element method. *Adv. Water Resour.* **136**, 103453 (2020).
27. Diersch, H. Finite element modelling of recirculating density-driven saltwater intrusion processes in groundwater. *Adv. Water Resour.* **11**, 25–43 (1988).
28. Frolkovič, P. & De Schepper, H. Numerical modelling of convection dominated transport coupled with density driven flow in porous media. *Adv. Water Resour.* **24**, 63–72 (2000).
29. Kolditz, O., Ratke, R., Diersch, H. & Zielke, W. Coupled groundwater flow and transport: 1. verification of variable density flow and transport models. *Adv. water resources* **21**, 27–46 (1998).
30. Amsallem, D., Zahr, M., Choi, Y. & Farhat, C. Design optimization using hyper-reduced-order models. *Struct. Multidiscip. Optim.* **51**, 919–940 (2015).
31. McBane, S. & Choi, Y. Component-wise reduced order model lattice-type structure design. *Comput. Methods Appl. Mech. Eng.* **381**, 113813 (2021).
32. Choi, Y., Oxberry, G., White, D. & Kirchdoerfer, T. Accelerating design optimization using reduced order models. *arXiv preprint arXiv:1909.11320* (2019).
33. Choi, Y., Boncoraglio, G., Anderson, S., Amsallem, D. & Farhat, C. Gradient-based constrained optimization using a database of linear reduced-order models. *J. Comput. Phys.* **423**, 109787 (2020).
34. Ballarin, F., D'Amario, A., Perotto, S. & Rozza, G. A POD-selective inverse distance weighting method for fast parametrized shape morphing. *Int. J. for Numer. Methods Eng.* **117**, 860–884 (2019).
35. Carlberg, K., Choi, Y. & Sargsyan, S. Conservative model reduction for finite-volume models. *J. Comput. Phys.* **371**, 280–314 (2018).
36. Venturi, L., Ballarin, F. & Rozza, G. A weighted POD method for elliptic PDEs with random inputs. *J. Sci. Comput.* **81**, 136–153 (2019).
37. Choi, Y. & Carlberg, K. Space-time least-squares Petrov-galerkin projection for nonlinear model reduction. *SIAM J. on Sci. Comput.* **41**, A26–A58 (2019).

38. Copeland, D., Cheung, S., Huynh, K. & Choi, Y. Reduced order models for lagrangian hydrodynamics. Comput. Methods Appl. Mech. Eng. **388**, 114259 (2022).
39. Hoang, C., Choi, Y. & Carlberg, K. Domain-decomposition least-squares petrov–galerkin (dd-lspg) nonlinear model reduction. Comput. Methods Appl. Mech. Eng. **384**, 113997 (2021).
40. Choi, Y., Brown, P., Arrighi, W., Anderson, R. & Huynh, K. Space–time reduced order model for large-scale linear dynamical systems with application to Boltzmann transport problems. J. Comput. Phys. **424**, 109845 (2021).
41. Kadeethum, T., Ballarin, F. & Bouklas, N. Data-driven reduced order modeling of poroelasticity of heterogeneous media based on a discontinuous galerkin approximation. GEM-International J. on Geomathematics **12**, 1–45 (2021).
42. DeCaria, V., Iliescu, T., Layton, W., McLaughlin, M. & Schneier, M. An artificial compression reduced order model. SIAM J. on Numer. Analysis **58**, 565–589 (2020).
43. Cleary, J. & Witten, I. Data compression using adaptive coding and partial string matching. IEEE transactions on Commun. **32**, 396–402 (1984).
44. Zbontar, J., Jing, L., Misra, I., LeCun, Y. & Deny, S. Barlow twins: Self-supervised learning via redundancy reduction. arXiv preprint arXiv:2103.03230 (2021).
45. Elder, J. Transient convection in a porous medium. J. Fluid Mech. **27**, 609–623 (1967).
46. Simpson, M. & Clement, T. Theoretical analysis of the worthiness of Henry and Elder problems as benchmarks of density-dependent groundwater flow models. Adv. Water Resour. **26**, 17–31 (2003).
47. Diersch, H. & Kolditz, O. Variable-density flow and transport in porous media: approaches and challenges. Adv. water resources **25**, 899–944 (2002).
48. Yoon, H., Valocchi, A., Werth, C. & Dewers, T. Pore-scale simulation of mixing-induced calcium carbonate precipitation and dissolution in a microfluidic pore network. Water Resour. Res. **48** (2012).
49. Yoon, H., Kang, Q. & Valocchi, A. Lattice boltzmann-based approaches for pore-scale reactive transport. Rev. Mineral. Geochem. **80**, 393–431 (2015).
50. Yoon, H., Chojnicki, K. & Martinez, M. Pore-scale analysis of calcium carbonate precipitation and dissolution kinetics in a microfluidic device. Environ. Sci. & Technol. **53**, 14233–14242 (2019).
51. Yoon, H. et al. Adaptation of delftia acidovorans for degradation of 2, 4-dichlorophenoxyacetate in a microfluidic porous medium. Biodegradation **25**, 595–604 (2014).
52. Inspectorate, S. N. P. The international hydrocoin project—background and results. Organ. for Econ. Co-operation Dev. Paris (1987).
53. Flemisch, B. et al. Benchmarks for single-phase flow in fractured porous media. Adv. Water Resour. **111**, 239–258 (2018).
54. Paul-Dubois-Taine, A. & Amsallem, D. An adaptive and efficient greedy procedure for the optimal training of parametric reduced-order models. Int. J. for Numer. Methods Eng. **102**, 1262–1292 (2015).
55. Vasile, M. et al. Adaptive sampling strategies for non-intrusive pod-based surrogates. Eng. computations (2013).
56. Raissi, M., Perdikaris, P. & Karniadakis, G. Physics-informed neural networks: A deep learning framework for solving forward and inverse problems involving nonlinear partial differential equations. J. Comput. Phys. **378**, 686–707 (2019).
57. Kadeethum, T., Jørgensen, T. M. & Nick, H. M. Physics-informed neural networks for solving nonlinear diffusivity and Biot’s equations. PloS one **15**, e0232683 (2020).
58. Huang, X., Liu, M., Belongie, S. & Kautz, J. Multimodal unsupervised image-to-image translation. In Proceedings of the European conference on computer vision (ECCV), 172–189 (2018).
59. Joseph, D. Stability of fluid motions I, vol. 27 (Springer Science & Business Media, 2013).
60. Chen, Z., Huan, G. & Ma, Y. Computational methods for multiphase flows in porous media, vol. 2 (Siam, 2006).
61. Lake, L., Johns, R., Rossen, B. & Pope, G. Fundamentals of enhanced oil recovery (Society of Petroleum Engineers Richardson, TX, 2014).
62. Wang, H., Ren, K. & Song, J. A closer look at batch size in mini-batch training of deep auto-encoders. In 2017 3rd IEEE International Conference on Computer and Communications (ICCC), 2756–2761 (IEEE, 2017).
63. Karras, T., Aila, T., Laine, S. & Lehtinen, J. Progressive growing of gans for improved quality, stability, and variation. arXiv preprint arXiv:1710.10196 (2017).

64. Kadeethum, T. et al. A framework for data-driven solution and parameter estimation of pdes using conditional generative adversarial networks. *Nat. Comput. Sci.* **1**, 819–829, DOI: <https://doi.org/10.1038/s43588-021-00171-3> (2021).
65. Kingma, D. & Ba, J. Adam: A method for stochastic optimization. *arXiv preprint arXiv:1412.6980* (2014).
66. Loshchilov, I. & Hutter, F. Sgdr: Stochastic gradient descent with warm restarts. *arXiv preprint arXiv:1608.03983* (2016).
67. Prechelt, L. Early stopping-but when? In *Neural Networks: Tricks of the trade*, 55–69 (Springer, 1998).
68. Prechelt, L. Automatic early stopping using cross validation: quantifying the criteria. *Neural Networks* **11**, 761–767 (1998).

Acknowledgements

TK and HY were supported by the Laboratory Directed Research and Development program at Sandia National Laboratories and US Department of Energy Office of Fossil Energy and Carbon Management, Science-Informed Machine Learning to Accelerate Real Time Decisions-Carbon Storage (SMART-CS) initiative. FB thanks the project “Numerical modeling of flows in porous media” funded by the Catholic University of the Sacred Heart, and the European Union’s Horizon 2020 research and innovation program under the Marie Skłodowska-Curie Actions, grant agreement 872442 (ARIA). DO acknowledges support from Los Alamos National Laboratory’s Laboratory Directed Research and Development Early Career Award (20200575ECR). YC acknowledges LDRD funds (21-FS-042) from Lawrence Livermore National Laboratory (LLNL-JRNL-831095). Lawrence Livermore National Laboratory is operated by Lawrence Livermore National Security, LLC, for the U.S. Department of Energy, National Nuclear Security Administration under Contract DE-AC52-07NA27344. NB acknowledges startup support from the Sibley School of Mechanical and Aerospace Engineering, Cornell University. Sandia National Laboratories is a multimission laboratory managed and operated by National Technology and Engineering Solutions of Sandia LLC, a wholly owned subsidiary of Honeywell International Inc. for the U.S. Department of Energy’s National Nuclear Security Administration under contract DE-NA0003525. This paper describes objective technical results and analysis. Any subjective views or opinions that might be expressed in the paper do not necessarily represent the views of the U.S. Department of Energy or the United States Government.

Author contributions statement

T. Kadeethum: Conceptualization, Formal analysis, Software, Validation, Writing - original draft, Writing - review & editing. **F. Ballarin:** Conceptualization, Formal analysis, Supervision, Validation, Writing - review & editing. **D. O’Malley:** Conceptualization, Formal analysis, Supervision, Validation, Writing - review & editing. **Y. Choi:** Conceptualization, Formal analysis, Supervision, Validation, Writing - review & editing. **N. Bouklas:** Conceptualization, Formal analysis, Funding acquisition, Supervision, Writing - review & editing. **H. Yoon:** Conceptualization, Formal analysis, Funding acquisition, Supervision, Writing - review & editing.

Competing interests

The authors declare no competing interests

Code and data availability

We will release our scripts and training and testing data to reproduce all results in the manuscript through the Sandia National Laboratories software portal — a hub for GitHub-hosted open source projects (<https://github.com/sandialabs>) after the manuscript will be accepted.